

Spatio-Spectral Quantum State Estimation of Photon Pairs from Optical Fiber Using Stimulated Emission

DONG BEOM KIM^{1,2*}, XIYE HU^{1,2}, ALFRED B. U'REN³, KARINA GARAY-PALMETT⁴, AND VIRGINIA O. LORENZ^{1,2}

¹*Department of Physics, University of Illinois Urbana-Champaign, Urbana, Illinois 61801, USA*

²*Illinois Quantum Information Science & Technology Center (IQIST), University of Illinois Urbana-Champaign, Urbana, Illinois 61801, USA*

³*Instituto de Ciencias Nucleares, Universidad Nacional Autónoma de México, A.P. 70-543, 04510 Ciudad de México, México*

⁴*Departamento de Óptica, Centro de Investigación Científica y de Educación Superior de Ensenada, B.C., 22860, Ensenada, México*

*dbkim3@illinois.edu

Abstract: Developing a quantum light source that carries more than one bit per photon is pivotal for expanding quantum information applications. Characterizing a high-dimensional multiple-degree-of-freedom source at the single-photon level is challenging due to the large parameter space as well as limited emission rates and detection efficiencies. Here, we characterize photon pairs generated in optical fiber in the transverse-mode and frequency degrees of freedom by applying stimulated emission in both degrees of freedom while detecting in one of them at a time. This method may be useful in the quantum state estimation and optimization of various photon-pair source platforms in which complicated correlations across multiple degrees of freedom may be present.

1. Introduction

Developing an efficient quantum light source [1, 2] that can carry more than one bit of information per photon is crucial for expanding quantum information applications in communication [3], computation [4], and metrology [5–7]. Optical fiber-based photon-pair sources [1] are an attractive platform that promises easy integration with existing fiber networks and correlations across multiple high-dimensional degrees of freedom (DOF) such as time, frequency, and transverse spatial mode [8–10].

Nevertheless, exploiting such multi-dimensionality requires non-trivial state characterization [1, 11, 12]. This characterization can be challenging to implement with conventional spontaneous-emission measurements including quantum state tomography (QST) [13]. The detection needs to span the entire multi-DOF space [8, 14, 15], potentially aided by extended QST methods such as adaptive quantum state tomography [16, 17], self-guided tomography [15, 18], and compressed sensing [19, 20]. Moreover, the involved coincidence-counting measurements often require single-photon sensitivity [21, 22], long integration times [8, 10], and a large number of projective measurements [14, 15].

Stimulated-emission tomography (SET) [12, 23–25] can speed up characterization through both stimulation and detection in multiple DOFs. The measurements employ classical seed light that stimulates the photon-pair generation process. The higher count rates of the stimulated process lead to more efficient tomography [23]. These stimulated measurements have been previously applied to a single DOF, such as polarization [25], frequency [23, 24, 26], and transverse spatial mode [27–30], and multiple DOFs including polarization-frequency [12] and polarization-path [31].

In this work, we extend this effort to introduce a multi-dimensional characterization method that can be applied to sources with correlations in multiple high-dimensional DOFs, in particular

transverse spatial mode and frequency. We utilize a few-mode polarization-maintaining fiber source that produces photon pairs correlated in transverse mode and frequency via spontaneous four-wave mixing (SFWM) [8–10]. We implement stimulated emission in multiple DOFs (transverse mode and frequency), but detect in one DOF at a time (transverse mode or frequency) [32]. We use a seed beam shaped in transverse-mode and frequency [27, 33–35] to stimulate the FWM process, and we measure the transverse-mode images and spectra of the stimulated signal using a camera and a spectrometer. Because the transverse modes and spectral modes are correlated, transverse-mode-resolved joint spectral intensities (JSIs) – an *inter*-DOF – can be used to investigate the transverse-mode quantum state – *intra*-DOF – of the photon pairs. The acquired inter-DOF coherence information can thus yield the intra-DOF coherence information.

This method reduces the number of measurements while still providing the coherence information across multiple DOFs. Our result also shows that stimulated emission imaging [27,29] can be achieved in fiber platforms, exhibiting a real-time monitoring capability. Consequently, this method can be used in conjunction with quantum state tomography to estimate the quantum state and diagnose the underlying causes of deviations from the target state in each DOF. Our method of extracting multi-dimensional information via stimulated emission using detection in one DOF can immediately aid in optimizing various photon-pair source platforms [1, 4, 36–40] where complicated correlations arise across multiple DOFs and generation processes.

We introduce the supported transverse-spatial modes, a theory on four-wave mixing, and the quantum state representation of the photon pairs generated from our few-mode polarization-maintaining optical fiber in Sec. 2. Then we describe the experimental setup and the procedure for our stimulated-emission characterization technique in Sec. 3. We present the main experimental results of transverse-mode-resolved JSI and how this compares to the spontaneous counterpart in Sec. 4. Finally, we discuss the implication of our characterization method by further implementing it in a shorter fiber that produces photon pairs with partial transverse-mode entanglement in Sec. 5. We estimate the quantum state of the photon pairs using our stimulated-emission method and compare it with that obtained by quantum state tomography.

2. Theory

2.1. Transverse spatial modes in few-mode polarization-maintaining optical fiber

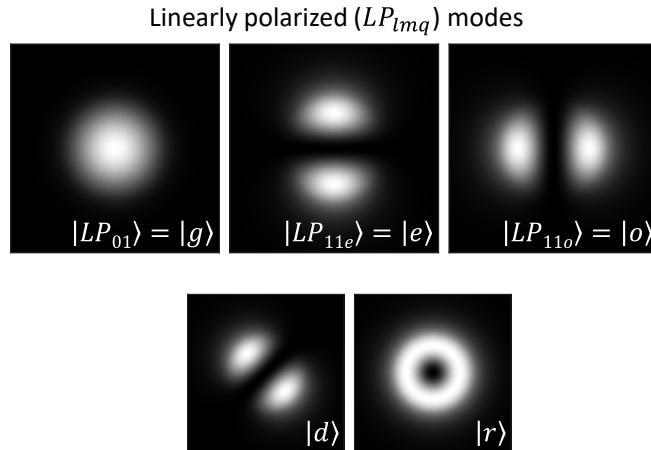


Fig. 1. Intensity distributions of the three linearly polarized (LP) modes supported in the PMF, $|g\rangle$, $|e\rangle$, and $|o\rangle$, and the two modes in superposition, $|d\rangle = (|e\rangle + |o\rangle)/\sqrt{2}$ and $|r\rangle = (|e\rangle + i|o\rangle)/\sqrt{2}$.

Linearly polarized modes (LP) are the transverse spatial modes supported in a conventional cylindrically-symmetric optical fiber that satisfies the weakly guided approximation [41]. These modes are denoted as LP_{lmq} , where l , m , and q are the azimuthal, radial, and parity indices describing its modal structure [9, 41]. In this paper, we consider a few-mode polarization-maintaining fiber (PMF) that supports three LP modes: $|LP_{01}\rangle = |g\rangle$, $|LP_{11e}\rangle = |e\rangle$, and $|LP_{11o}\rangle = |o\rangle$ (see Fig. 1). As transverse-mode basis states, these three LP modes can be combined to form superposition states, e.g., $|d, a\rangle = (|e\rangle \pm |o\rangle) / \sqrt{2}$ and $|r, l\rangle = (|e\rangle \pm i|o\rangle) / \sqrt{2}$ as shown in Fig. 1. The modes are then further affected by the two types of birefringence in the PMF: a polarization birefringence $\Delta = n^x - n^y$ between the slow (x) and the fast (y) axis of the PMF and a parity birefringence $\Delta^P = n^o - n^e$ between transverse modes with even (e) and odd (o) parities. The inset in Fig. 2 shows how the slow (x) axis of the PMF is oriented along the vertical with the intensity lobes of the mode $|e\rangle$ to form along the same direction.

When characterizing a photon-pair generation process in a few-mode PMF, it is important to accurately describe the property of a transverse mode at a given wavelength. For this purpose, we define an effective refractive index, which takes into account the transverse geometrical effect of the optical fiber (T_ν) as well as its material dispersion property (ω_ν): $n_\nu^{T_\nu} = n_{\text{eff}}(\omega_\nu, T_\nu)$ where T_ν and ω_ν are the transverse mode and the frequency of a given photon ν (= pump p , signal s , and idler i). Using this convention in xx - yy cross-polarized scheme [9, 42], where the pump is polarized along x and signal and idler are polarized along y , the effective refractive indices of the $|e\rangle$ and $|o\rangle$ modes can be represented as the following: $n_p^{ex} = n_p^e + \Delta$, $n_p^{ox} = n_p^o + \Delta^P$, $n_{s,i}^{ey} = n_{s,i}^e$, and $n_{s,i}^{oy} = n_{s,i}^o + \Delta^P$.

2.2. Four-wave mixing in few-mode polarization-maintaining optical fiber

Utilizing the transverse modes, the few-mode PMF can generate photon pairs correlated in transverse mode and frequency [8–10] through a nonlinear optical process called four-wave mixing (FWM). The FWM process relies on the $\chi^{(3)}$ nonlinear optical susceptibility of the fiber to annihilate two pump photons (p_1, p_2), leading to the emission of a signal (s) and an idler (i) photon pair. For this nonlinear process to occur, it needs to satisfy a phase-matching condition, which is determined by the energy ($\Delta\omega = 0$) and momentum conservation ($\Delta k = 0$) constraints, with

$$\begin{aligned} \Delta\omega &= \omega_{p_1} + \omega_{p_2} - \omega_s - \omega_i, \\ \Delta k &= k_{p_1} + k_{p_2} - k_s - k_i - k_{NL} \\ &= n(\omega_{p_1}, T_{p_1}) \frac{\omega_{p_1}}{c} + n(\omega_{p_2}, T_{p_2}) \frac{\omega_{p_2}}{c} - n(\omega_s, T_s) \frac{\omega_s}{c} - n(\omega_i, T_i) \frac{\omega_i}{c} - k_{NL}, \end{aligned} \quad (1)$$

where ω_ν , T_ν , k_ν are the angular frequency, transverse mode, and wavenumber (= $i\gamma$, γ is the propagation constant) of $\nu = \{p_1, p_2, s, i\}$, c the speed of light, and k_{NL} the nonlinear contribution from self- and cross-phase modulation [42]. Among the different types of FWM that Eq. 1 can represent, in this paper, we concentrate on cross-polarized birefringent phase-matching with frequency-degenerate pumps, of relevance in our experiments. The pumps satisfying $\omega_p = \omega_{p_1} = \omega_{p_2}$ are orthogonally polarized to the signal and idler in the PMF to take advantage of the reduced Raman scattering noise and the number of possible FWM processes [42–44].

Additionally, since the effective refractive index $n(\omega_\nu, T_\nu)$ depends on the transverse mode (T_ν) and frequency (ω_ν), the phase-matching condition in Eq. 1 will vary for different combinations of the two. This can lead to photon pairs with dissimilar transverse modes to acquire distinct frequency components (see Sec. 4). Thus, to emphasize the varying phase-matching condition, we use Δk_j for a FWM process j , where the corresponding transverse- and frequency modes are specified accordingly.

2.3. Quantum state representation of photon pairs

With the fundamentals of the transverse modes and FWM introduced, we can now express the quantum state $|\psi_{si}\rangle$ of the photon pair created from the few-mode PMF. Assuming cross-polarized birefringent phase-matching and frequency-degenerate pumps, the signal-idler photon pair $|\psi_{si}\rangle$ can be generated in a superposition of N distinct FWM processes as,

$$|\psi_{si}\rangle = \sum_j^N \int d\omega_s d\omega_i c_j |\omega_s \omega_i, T_s T_i, yy, \dots\rangle_j = \sum_j^N C_j \otimes |T_s T_i\rangle_j, \quad (2)$$

where the prefactors weighting each process j are

$$c_j = M_{c_j} \sqrt{P_{p1j} P_{p2j}} f_j(\omega_s, \omega_i) O_j(T_{p1}, T_{p2}, T_s, T_i), \quad C_j = \int d\omega_s d\omega_i c_j |\omega_s \omega_i, yy, \dots\rangle_j. \quad (3)$$

Here, $|\omega_s \omega_i, T_s T_i, yy, \dots\rangle_j$ represents the signal-idler state from process j in transverse mode, frequency, polarization, and other implicit degrees of freedom, e.g., position, time, etc. This expression is simplified as $C_j \otimes |T_s T_i\rangle_j$ to highlight the transverse-mode contribution. The prefactors c_j and C_j , which determine the relative amplitude and phase of each FWM process, are functions of average pump power $P_{p1,2j}$, joint spectral amplitude (JSA) $f_j(\omega_s, \omega_i)$, and transverse-mode overlap integral $O_j(T_{p1}, T_{p2}, T_s, T_i)$ [9]. M_{c_j} is the normalization constant satisfying $\langle \psi_{si} | \psi_{si} \rangle = 1$.

The JSA $f_j(\omega_s, \omega_i)$, which contains the information of spectral correlation or factorability between signal and idler photons for each FWM process [1, 8–11, 45], is defined and linearly approximated as,

$$f_j(\omega_s, \omega_i) = \int d\omega_p \alpha(\omega_p) \alpha(\omega_s + \omega_i - \omega_p) \phi_j(\omega_s, \omega_i) \approx \alpha(\omega_s, \omega_i) \phi_j(\omega_s, \omega_i), \quad (4)$$

where $\alpha(\omega_s, \omega_i)$ is the pump spectral envelope function and $\phi_j(\omega_s, \omega_i)$ is the phase-matching function for the process j . For degenerate pumps, the JSA can be linearly approximated to $f_j(\omega_s, \omega_i) \approx \alpha(\omega_s, \omega_i) \text{sinc}(\frac{L}{2} \Delta k_j) e^{i\frac{L}{2} \Delta k_j}$ where L is the length of the fiber and Δk_j is the phase mismatch for the process j as defined in Eq. 1. For non-degenerate pumps, on the other hand, while the JSA can be linearly approximated in the same multiplication form of Eq. 4, its expression is in a little more involved form as a function of the temporal walk-off between the two pumps [42]. In our system, $\alpha(\omega_s, \omega_i)$ and $\phi_j(\omega_s, \omega_i)$ describe the spectral widths of the JSA peak along the diagonal and anti-diagonal directions, respectively [42]. In this paper, we measure the joint spectral intensity (JSI) $|f_j(\omega_s, \omega_i)|^2$. The joint spectral phase (JSP) is defined as $\arg\{f_j(\omega_s, \omega_i)\}$. The transverse-mode overlap integral $O_j(T_{p1}, T_{p2}, T_s, T_i)$, on the other hand, quantifies the spatial overlap of the four transverse modes participating as defined in [9]. See Supplement 1 for a more comprehensive explanation of the factors in Eq. 3 and of the quantum state representation of the pump similar to Eq. 2.

With three transverse modes ($|g\rangle$, $|e\rangle$, and $|o\rangle$) for the pump, signal, and idler, and the fiber parameters for the PMF considered here (Fibercore HB800C) – obtained through the genetic algorithm analysis in [8]: fiber core radius $r = 1.74 \mu\text{m}$, numerical aperture $NA = 0.17$, $\Delta = 2.37 \times 10^{-4}$, $\Delta^p = 4.41 \times 10^{-4}$ –, only 10 out of 15 FWM processes satisfy the orbital angular momentum (OAM) and parity conservation and therefore are experimentally realizable [8, 9]. With only the $|e\rangle$ and $|o\rangle$ modes, 5 of the above FWM processes are viable with the following transverse mode combinations $(T_{p1}, T_{p2}, T_s, T_i)$: (e, e, e, e) , (e, o, e, o) , (o, e, o, e) , (o, o, o, o) , and (o, o, e, e) .

Using the formalism introduced earlier in Eqs. 2 and 3, these five FWM processes can be derived with pump $|\psi_p\rangle$ in a superposition of $|e\rangle$ and $|o\rangle$ transverse modes: $|\psi_p\rangle = A_e |e_p\rangle + A_o |o_p\rangle$.

The quantum states of the two pumps $|\psi_{p_1 p_2}\rangle$ and the signal-idler photon pair $|\psi_{si}\rangle$ can be represented as

$$\begin{aligned} |\psi_{p_1 p_2}\rangle &= |\psi_p\rangle^{\otimes 2} = B_{ee} |e_{p_1} e_{p_2}\rangle + B_{eo} |e_{p_1} o_{p_2}\rangle + B_{oe} |o_{p_1} e_{p_2}\rangle + B_{oo} |o_{p_1} o_{p_2}\rangle \\ &= B_{ee} |e_{p_1} e_{p_2}\rangle + 2B_{eo} |e_{p_1} o_{p_2}\rangle + B_{oo} |o_{p_1} o_{p_2}\rangle, \\ |\psi_{si}\rangle &= C_{ee} |e_s e_i\rangle + C_{eo} |e_s o_i\rangle + C_{oe} |o_s e_i\rangle + C_{oo} |o_s o_i\rangle, \end{aligned} \quad (5)$$

where A_j and B_j are prefactors of pump similar to C_j (see Supplement 1 for details). Here, \otimes between A_j, B_j, C_j and $|\dots\rangle_j$ are omitted for simplicity. Notice that $B_{eo} |e_{p_1} o_{p_2}\rangle = B_{oe} |o_{p_1} e_{p_2}\rangle$ is obeyed due to their indistinguishability and results in an extra factor of 2 before the B_{eo} term and implicitly in the corresponding signal-idler state terms, C_{eo} and C_{oe} through $P_{p_1,2j}$ in Eq. 3.

Given the photon-pair state in Eq. 5, stimulated emission of the FWM processes is an efficient way to characterize the state using either the signal or idler as a seed to stimulate the generation of the other. The stimulated emission benefits from the linear proportionality of the stimulated photon number to the seed photon number multiplied by the spontaneous photon-pair number [23, 24]. In addition, if the transverse modes of the pump and the seed can be controlled simultaneously with their frequencies, the individual FWM processes, and thus the photon-pair state in Eq. 5, can be selectively excited with high efficiency [12, 32]. This is equivalent to applying a projection operator $|\omega_i, T_i, y\rangle_{j_0} \langle \omega_i, T_i, y|_{j_0}$, corresponding to seeding with an idler state of a FWM process j_0 , to $|\psi_{si}\rangle$ in Eq. 2 and 5 to obtain the stimulated photon state $|\omega_s, T_s, y\rangle_{j_0}$. Indeed, this requires a sufficiently well-defined pump (T_{p_1}, T_{p_2}) and seed transverse modes (T_i) along with a narrow spectral bandwidth seed (ω_i), as will become clear in the following sections.

3. Methods

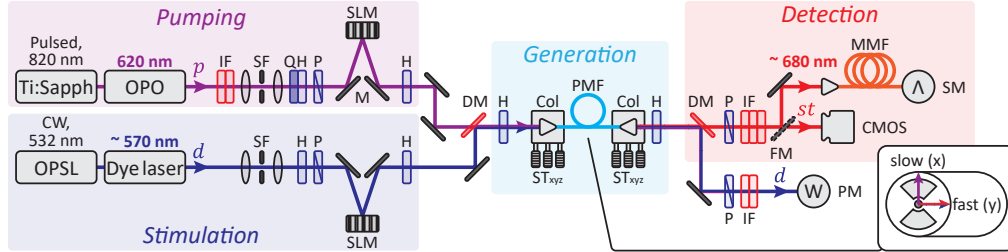


Fig. 2. Experimental setup. The transverse-mode-frequency structured pump (seed) beam generates (stimulates) a particular photon-pair state in optical fiber that is further detected with the spectrometer or the CMOS camera. The inset shows the slow (x) and fast (y) axes of the PMF. p : pump, d : seed, st : stimulated signal, IF: interference filter, SF: spatial filter consisting of a pinhole and a convex lens, Q: quarter-wave plate, H: half-wave plate, P: linear polarizer, M: mirror, SLM: spatial light modulator, DM: dichroic mirror, Col: collimator, ST_{xyz} : xyz-translation stage, PMF: polarization-maintaining fiber, FM: flip mirror, SM: spectrometer, PM: power meter.

We use the experimental setup shown in Fig. 2 to characterize our fiber-based photon-pair source via stimulated-emission, similar to [23, 24]. Here, the photon-pair state is analyzed in both transverse mode and wavelength. The pump beam is pulsed with 8 mW power and ≈ 200 fs duration, centered at 620 nm, which is generated from an optical parametric oscillator (OPO, Inspire HF100) pumped by a pulsed Ti:Sapphire laser (Mai Tai HP). This pump is coupled into a 10 cm-long few-mode polarization-maintaining fiber (PMF, HB800C, Fibercore) and polarized along the slow-axis (x) to create signal-idler photon pairs via cross-polarized

FWM, as described in Sec. 2. To stimulate these FWM processes, a 2 mW seed beam that is wavelength-tunable around 570 nm with 2 GHz linewidth is sent into the same PMF and polarized along the fast-axis (y). This seed beam is generated from a continuous wave (CW) ring dye laser (Coherent 899) pumped with a CW optically pumped semiconductor laser (OPSL, Verdi G20). The transverse-mode, frequency, and polarization state of the seed is utilized to selectively stimulate a specific FWM process defined by a given pump; note that precise control of the transverse modes and the wavelengths is crucial.

For transverse-mode control, both the pump and the seed beams are shaped to the desired modes (Fig. 2) with reflective phase-only spatial light modulators (SLM, Holoeye Pluto 2). In Sec. 4, the pump is shaped [46] to $|d\rangle$ and the seed to $|e\rangle$, $|o\rangle$, and $|d\rangle$. In addition to the standard methods of using a computer-generated SLM phase mask for transverse-mode control [21, 33–35, 47, 48], the phase mask is adjusted iteratively by monitoring the spontaneous or stimulated FWM spectrum to selectively excite one FWM process (spectral peak) at a time. Spectrally, the seed is calibrated by measuring its center wavelength as a function of the DC servo motor (Thorlabs Z812B) position, which is responsible for the wavelength tuning of the dye laser. Supplement 1 shows the result of this calibration in servo motor steps of 0.1 mm. Note that the polarization optics, interference filters, and pinhole-spatial filters across the experimental setup further prepare the beams to accurately excite FWM processes. The interference filters spectrally filter the pump to about 2 nm in full-width half maximum around 620 nm and the stimulated signal to a range of about (670 to 700) nm.

After the calibration process, the pump and the seed with chosen transverse modes and wavelengths are coupled into the PMF to generate stimulated photons via FWM. For a given seed wavelength, these stimulated photons are then spectrally filtered and measured in two degrees of freedom (switchable via a flip mirror): wavelength with a spectrometer (Andor SR303i with iDus 420) and transverse mode with a CMOS camera (Thorlabs CS505MU) which uses a $16 \text{ px} \times 16 \text{ px}$ pixel-binning. Following the data normalization with a seed power measured at the PMF output using a power meter, this process is repeated for the seed wavelength range of about (567 to 576) nm in steps of 0.05 nm, or 0.01 mm in the servo motor position.

4. Results

4.1. Transverse-mode-resolved joint spectral intensity

Using the methods described in Sec. 3, we resolve different FWM processes supported in the few-mode PMF both spectrally and spatially. Fig. 3 shows the reconstructed joint spectral intensity (JSI) plots of the photon pairs and the transverse-mode images of the stimulated signal photons measured for this analysis. The transverse mode images are taken with the camera exposure times of 200 ms for Fig. 3(a-b) and 400 ms for Fig. 3(c) after filtering with narrow spectral filters to isolate individual FWM processes. The states of the stimulated signal (st) and the seed (d) describe those of the signal (s , around 680 nm) and the idler (i , around 570 nm) photons in the FWM processes, respectively.

Fig. 3(a-c) show how varying the seed transverse modes to $|e\rangle$, $|o\rangle$, and $|d\rangle$ while keeping the pump mode at $|d\rangle = (|e\rangle + |o\rangle)/\sqrt{2}$ changes the JSI and the transverse-mode of the stimulated signal. This helps isolate different FWM processes based on the seed transverse mode and determine the corresponding stimulated transverse mode. Specifically, only the FWM processes that involve the given idler (seed) transverse mode are stimulated and expressed as individual spectral peaks in the JSI plots. For example, in Fig. 3(a (b)), the processes at A and C (B and D), which require a $|e\rangle$ ($|o\rangle$) seed, are excited even with the same $|d\rangle$ pump. On the other hand, when the seed transverse mode is in a superposition of the two as in Fig. 3(c), all of the four FWM processes are excited, effectively superposing processes in Fig. 3(a) and (b). From these results, we can conclude that within the given spectral range, a $|d\rangle$ pump can create a photon pair from the four possible FWM processes (labeled as A, B, C, and D) with the following transverse-

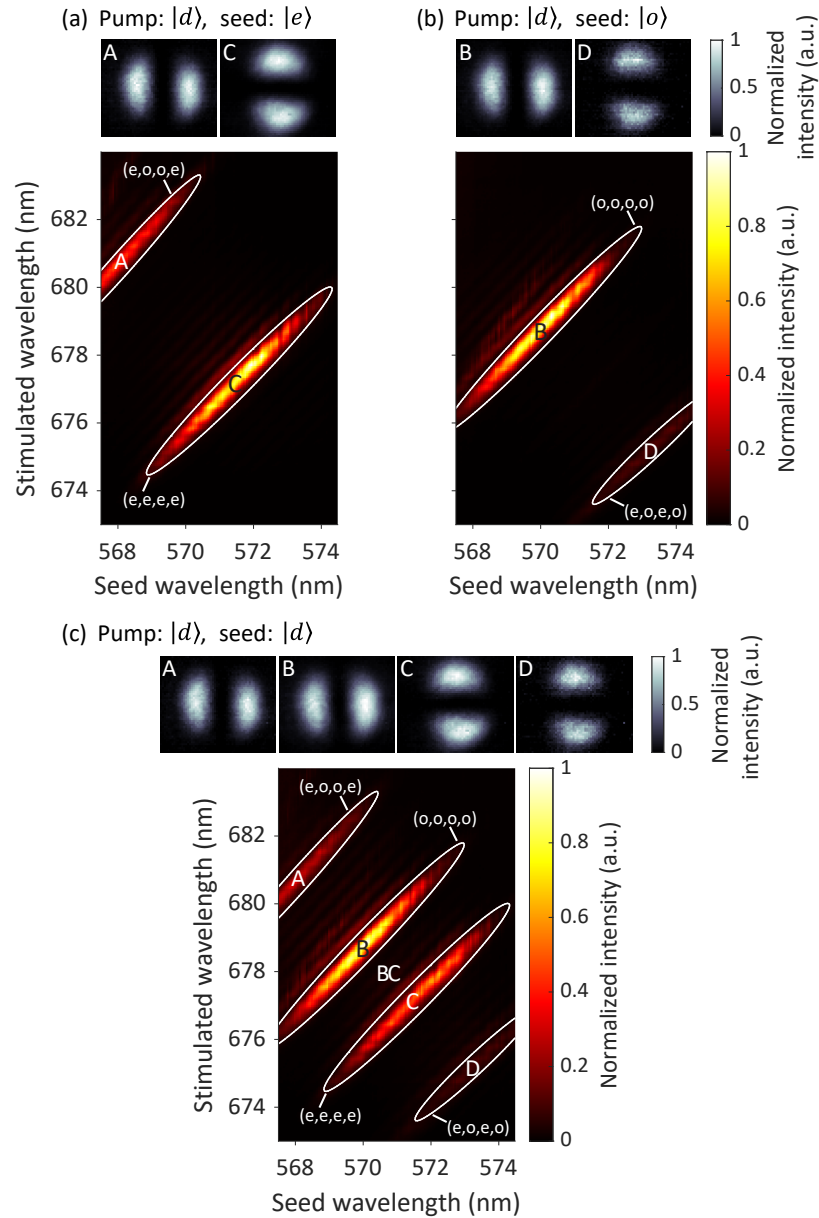


Fig. 3. Transverse-mode images of the stimulated signal (top) and joint spectral intensity (JSI) plots (bottom) for different seed transverse modes, (a) $|e\rangle$, (b) $|o\rangle$, and (c) $|d\rangle$, and FWM processes (A-D). The pump transverse mode is fixed to $|d\rangle$. Each FWM process (A-D) with transverse modes $(T_{p_1}, T_{p_2}, T_s, T_i)$ is specified with a $1/e^3$ contour (solid line) of the two-dimensional Gaussian fit. The transverse mode images are captured with camera exposure times of (a-b) 200 ms and (c) 400 ms at the JSI peaks with narrow stimulated signal spectral filters to block other FWM contributions. The intensities of all transverse mode images and JSI plots are normalized to one. See Visualization 1 and 2 for a real-time video and an animation that show the continuous evolution of the stimulated transverse mode as the seed wavelength is scanned.

mode combinations $|T_s T_i\rangle_j$: $|o_s, e_i\rangle_A$, $|o_s, o_i\rangle_B$, $|e_s, e_i\rangle_C$, and $|e_s, o_i\rangle_D$. The processes are observed at the center signal and idler wavelengths $(\lambda_s, \lambda_i)_j$ obtained from a Gaussian fit of the corresponding process JSI's: $(680.7, 568.1)_A$ nm, $(678.7, 570.0)_B$ nm, $(677.2, 571.6)_C$ nm, and $(675.3, 573.3)_D$ nm. Through further measurements with $|e\rangle$ and $|o\rangle$ pumps and the information from Sec. 2, the required pump transverse modes for each FWM process $(T_{p1}, T_{p2}, T_s, T_i)$ can be determined: $(e_{p1}, o_{p2}, o_s, e_i)_A$, $(o_{p1}, o_{p2}, o_s, o_i)_B$, $(e_{p1}, e_{p2}, e_s, e_i)_C$, and $(e_{p1}, o_{p2}, e_s, o_i)_D$. Hence, controlling the seed transverse mode enables a selective FWM stimulation and facilitates a more comprehensive characterization.

This characterization capability is instrumental in assessing the degree of spectral overlap among FWM processes, which is pivotal for creating transverse-mode entanglement. Notice that, these processes are spectrally separated in the joint spectral space due to different phase matching conditions from unequal effective refractive indices of transverse modes as explained in Sec. 2. This means that the quantum state of the signal-idler photon pair, $|\psi_{si}\rangle = \sum_j \int d\lambda_s d\lambda_i c_j |T_s T_i, \lambda_s \lambda_i\rangle_j$ in transverse-spectral-mode, becomes a mixed state in the transverse-mode domain by tracing over the spectral degree of freedom to form a reduced density matrix, i.e., $\rho_{si}^T = \text{tr}_\lambda(\rho_{si}) = \sum_j C_j |T_s T_i\rangle_j \langle T_s T_i|_j$. Here, j denotes the FWM processes in A, B, C, and D. Physically, this signifies that the FWM processes cannot interfere with each other in the same manner that two classical light modes with different wavelengths cannot.

Note, however, that when sufficiently widening the signal spectral filtering window to let all of the 4 FWM processes through, the stimulated transverse mode image obtained at the seed wavelength of $\lambda_d = 570.8$ nm, to be referred to as BC (in between the processes B and C) in our Visualization 1 data sequence, shows an interesting “superposition” behavior: a *donut* mode (intensity null at the center), often associated with an orbital angular momentum mode [36, 49], or a superposition mode $|r\rangle = (|e\rangle + i|o\rangle)/\sqrt{2}$ when expressed in the LP mode basis (see Fig. 1). In fact, an incoherent mixture (a mixed state) of the $|e\rangle$ and $|o\rangle$ modes, $(|e\rangle\langle e| + |o\rangle\langle o|)/2$, also exhibits an identical intensity distribution as the coherently *mixed* superposition state, $|r, l\rangle = (|e\rangle \pm i|o\rangle)/\sqrt{2}$. Thus, solely imaging the stimulated transverse-mode at BC with a $|d\rangle$ seed may not give enough information to solve the ambiguity. Fortunately, a possible misinterpretation can be avoided through our transverse-mode-resolved JSI measurements. The additional information from Fig. 3(a-b) implies that the donut mode is likely the result of a spectrally distinguishable, incoherent mixture of the two stimulated signal transverse modes, $|o\rangle$ and $|e\rangle$, from processes B and C. Thus, the donut mode at BC in Fig. 3(a) manifests that these two FWM processes can be simultaneously excited at $(\lambda_d = 570.8$ nm) with two separate signal wavelengths. Similarly, benefiting from our real-time monitoring capability (see Visualization 2 data sequence), measuring the change in the stimulated transverse mode while changing the phase of the pump or the seed beam may also reveal the coherence property of the involved FWM processes.

Our technique is also useful in revealing additional underlying physics in the fiber-based photon-pair system when utilized in conjunction with the numerical simulation [8, 9]. An example is the parity birefringence dispersion δ necessary for explaining the spectrally separated FWM processes at B and C in Fig. 3. Without such correction, the numerical simulation may incorrectly predict the two FWM processes to completely overlap spectrally, allowing a transverse-mode entanglement [38]. For simplicity, we assume δ is a constant that describes the difference between the signal and the idler parity birefringences, i.e., $\delta = \Delta_s^p - \Delta_i^p$. Then, $\delta \sim 3 \times 10^{-5}$, which is an order of magnitude smaller than Δ^p , best describes the experimental results (compare Fig. 3(c) and 4(c)). While the discrepancies between the experiment and the numerical simulation arise due to rough estimation of the fiber parameters, more accurate analysis using a full genetic algorithm calculation may be implemented to improve the agreement [8, 9]. The second example is the transverse-mode overlap integral factor $O_j(T_{p1}, T_{p2}, T_s, T_i)$ in Eq. 3 that can explain the relative intensity difference observed among the FWM processes in Fig. 3 JSI plots. As shown in Eq. 3,

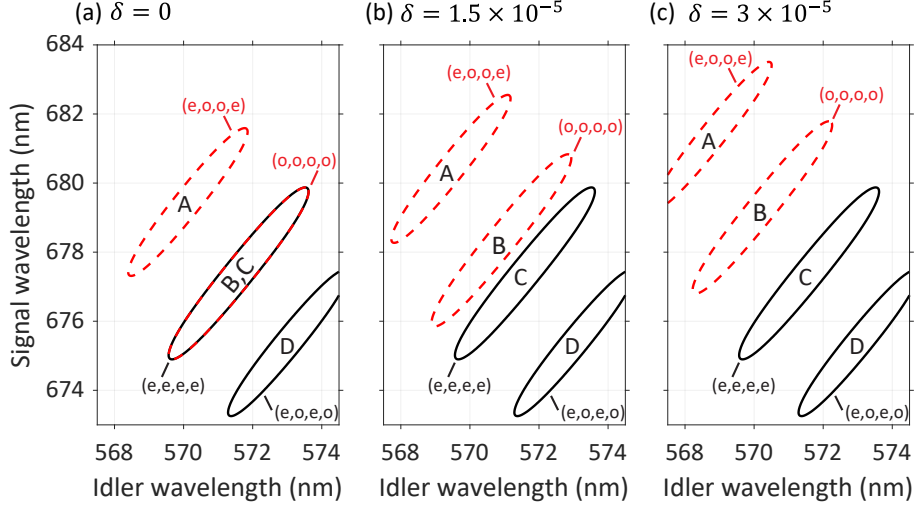


Fig. 4. Numerically simulated joint spectral intensity (JSI) plots with varying parity birefringence dispersion, δ : (a) 0, (b) 1.5×10^{-5} , and (c) 3×10^{-5} . The $1/e^3$ contours (solid and dashed) show the spectral distribution of the labeled SFWM processes (A-D), $(T_{p_1}, T_{p_2}, T_s, T_i)$. Increasing the parity birefringence dispersion δ increases the spectral separation between C (e,e,e,e) and B (o,o,o,o) by translating the two SFWM processes A (e,o,o,e) and B (o,o,o,o) (dashed), towards the top left. The pump is in $|d\rangle$.

this overlap integral O_j affects the photon-pair generation efficiency of a FWM process j [9]. $|O_j|^2$, which is proportional to the relative intensity of the JSI, is maximal ($|O|^2 \approx 0.35$) when all the participating transverse modes are identical and smaller by a factor of about 2.2 ($|O|^2 \approx 0.15$) when there are two $|e\rangle$'s and two $|o\rangle$'s (see Supplement 1 for more details on the calculation). This explains why the FWM processes in Fig. 3 at B ($o_{p_1}, o_{p_2}, o_s, o_i$) and C ($e_{p_1}, e_{p_2}, e_s, e_i$) appear brighter compared to those at A ($e_{p_1}, o_{p_2}, o_s, e_i$), and D ($e_{p_1}, o_{p_2}, e_s, o_i$). Additional asymmetry in intensity between the processes at B and C (see Fig. 3(c)) can be explained by the unaccounted pump ($\sqrt{P_{p_1} P_{p_2}}$ in Eq. 3) or the seed power difference for the $|e\rangle$ and $|o\rangle$ modes across the wavelength range.

4.2. Transverse mode imaging method comparison

To demonstrate the efficiency of our stimulated-emission imaging, we compare the transverse-mode images of the signal with and without the seed, i.e., using stimulated and spontaneous FWM. This is achieved by simply blocking or unblocking the beam path of the seed in our experimental setup (Fig. 2).

The stimulated-emission imaging is beneficial in obtaining a higher contrast image more efficiently. Fig. 5(a) shows a transverse-mode image of a signal from spontaneous FWM taken with an exposure time of 14235 ms, the longest available with our CMOS camera. With a shorter exposure time of 400 ms, it does not exhibit any noticeable spatial structure above the background counts. With this same shorter exposure time of 400 ms (≈ 36 times smaller than that used in the spontaneous case), however, the stimulated image in Fig. 5(b) shows a much clearer mode structure with less background noise. This is consistent with the previous studies [23, 24] that showed stimulated-emission-based characterization enables more efficient measurement of single-photon-level states. With this efficiency, remarkably, even a real-time monitoring of a changing transverse mode is possible as shown in our Visualization 2 data sequence, similar to [29].

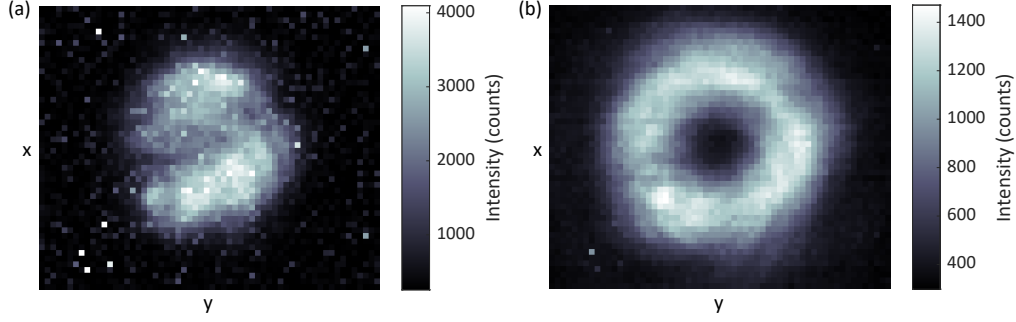


Fig. 5. Transverse-mode images of the signal from (a) spontaneous (without seed) FWM with an exposure time of 14235 ms and (b) stimulated FWM (with $|d\rangle$ seed) with an exposure time of 400 ms. In both cases, the pump is in $|d\rangle$ transverse mode and the spectral filters on the signal path are adjusted such that they transmit all 4 FWM processes. Stimulated signal image corresponds to a vertical slice of the JSI at BC in Fig. 3(c). The intensities of the images are in raw counts as shown on the camera software.

Moreover, stimulated-emission imaging is advantageous in resolving and identifying the seemingly intermingled multi-dimensional FWM processes, especially as exhibited in our few-mode PMF. Directly imaging a spontaneously emitted signal yields a single image as shown in Fig. 5(a), making it hard to distinguish the individual contributions from different FWM processes, if more than one exists within the spectral window of interest. While it is possible to spectrally resolve these processes and transverse modes with narrow-band spectral filters as in [8, 22], it entails multiple complications: longer measurement times, additional equipment for single-photon-level transverse-mode measurement, and coincidence counting to overcome the low contrast. In contrast, with stimulated imaging, different signal transverse modes can be imaged through a controlled choice of the seed transverse mode and wavelength (see Fig. 3), helping to deliver a fuller transverse-mode-spectral relationship of the photon pairs created from the multi-FWM PMF.

In addition, stimulated imaging is a more robust technique that facilitates more accurate probing and depiction of the transverse modes. The spontaneous image in Fig. 5(a) exhibits a transverse mode that resembles the pump mode $|d\rangle$, which is slightly different than the donut mode expected from an incoherent mixture of spectrally distinguishable FWM processes shown in Fig. 3. This ambiguity in Fig. 5(a) spontaneous image can be attributed to the Raman scattering which can be a dominant feature in the SFWM processes with higher order transverse modes [44]. With the experimental parameters used here, not only do this Raman noise and FWM signal spectrally overlap, but they also have comparable spectral strength. To further identify the underlying cause in the future experiments, idler transverse-mode imaging with potentially less Raman contamination than that of the signal [44], pixel-by-pixel coincidence counting [8, 22], or ghost imaging-type of measurement [5–7], involving a camera triggered with a bucket detector on the idler path to detect the signal photons, can be employed [1]. On the contrary, the stimulated-emission imaging can amplify the signal well above the Raman noise floor as shown in Fig. 5(b), yielding a high signal-to-noise ratio image required to retain the aforementioned advantages over the spontaneous imaging.

5. Application

5.1. Transverse-mode quantum state estimation from transverse-mode-resolved JSIs

With the advantages described in Sec. 4, we apply stimulated-emission to characterize a fiber source that possesses a partial transverse-mode entanglement. This characterization not only helps us identify the FWM processes based on their frequencies and transverse-modes, but also allows us to numerically estimate the single-DOF, transverse-mode quantum state of the photon pairs created. Throughout this process, we may find the potential causes that degrade the transverse-mode entanglement and optimize the source accordingly.

For this analysis, we employ a shorter but orthogonally-polarized PMF (2.5 cm×2, HB800C) [50] along with the same experimental setup used in Sec. 3. The shorter fiber induces more spectral overlap (indistinguishability) across different FWM processes. The smaller the fiber length L , the wider the spectral bandwidth of the phase-matching function $\phi(\omega_s, \omega_i)$ across the anti-diagonal direction in the JSI, resulting in a larger spectral region exhibiting overlap (see Sec. 2.3). Our initial goal was to create a maximally entangled transverse-mode Bell state [51, 52], $|\psi_{si}\rangle = (|e_s e_i\rangle + |o_s o_i\rangle) / \sqrt{2}$, necessitating indistinguishability between $|e_s e_i\rangle$ and $|o_s o_i\rangle$ in all other degrees of freedom, i.e., $C_{ee} = mC_{oo}$ (see Eq. 3), where m is a constant. Consequently, the JSIs (Eq. 4) need to satisfy the following overlap condition at the desired frequencies, ω_s and ω_i : $|f_{ee}(\omega_s, \omega_i)|^2 = |f_{oo}(\omega_s, \omega_i)|^2$.

Under these conditions, we measure transverse-mode resolved JSIs as described in Sec. 3. Fig. 6(a) shows this JSI with the pump in $|d\rangle$ and the seed in $|a\rangle$, where we identify the transverse modes of the FWM peaks and label them with the FWM processes: $(T_{p1}, T_{p2}, T_s, T_i) = A (e_{p1}, o_{p2}, o_s, e_i)$, B $(o_{p1}, o_{p2}, o_s, o_i)$, C $(e_{p1}, e_{p2}, e_s, e_i)$, and D $(e_{p1}, o_{p2}, e_s, o_i)$. To identify the processes, we conduct a series of measurements similar to Fig. 3 with 5 different transverse-mode combinations (pump-seed transverse-modes of $e-e$, $o-o$, $d-e$, and $d-o$). The solid curves in Fig. 6(a) represent the $1/e^2$ contours of the two-dimensional Gaussian curve fittings (goodness of fit $R^2 \approx 0.9$) as in Sec. 4. As these contours show some spectral overlap between processes B and C at the intersection, some transverse-mode entanglement can be expected here.

Compared to Fig. 3(a-c), in Fig. 6(a), the four processes A, B, C, and D are positioned much closer to each other with some clear overlap between B and C. Even for the same type of fiber, HB800C, the fiber parameters can differ from spool-to-spool, which may result in different FWM peak positions observed. Here, given that the Fig. 3(a-c) and 6(a) fibers are from different spools, we identify that this shorter PMF should have a smaller parity birefringence $\Delta^p \sim 1 \times 10^{-4}$.

Before using this JSI to estimate the transverse-mode quantum state, as a reference, we measure the same state using a conventional transverse-mode quantum state tomography (QST) [13]. Specifically, we install an additional SLM, pairs of single-mode fibers and single-photon detectors, and a coincidence counter at the *detection* part of the setup in Fig. 2 to project the signal-idler transverse-mode states into six mutually unbiased measurement basis states and conduct 36 coincidence measurements [13, 36, 52–55]. Fig. 6(b) shows the measured ρ_{QST} with partial transverse-mode entanglement characterized by a non-zero entanglement measure, concurrence = 0.27 ± 0.03 . Yet, due to the non-zero $|o_s e_i\rangle$ and $|e_s o_i\rangle$ components in the density matrix, the similarity with the target Bell state is not 1, i.e., yielding a Bell fidelity of 0.48 ± 0.02 . It also exhibits a non-unity purity = 0.52 ± 0.01 associated with a classical mixture contribution (no off-diagonal components) from states $|o_s e_i\rangle$ and $|e_s o_i\rangle$. The errors presented here are computed from 10^2 randomly sampled density matrices assuming that the coincidence counts in the QST measurement follow the Poisson distribution.

Now we estimate the transverse-mode density matrix from the transverse-mode-resolved JSI, and compare with the measured ρ_{QST} . We characterize the transverse-mode density matrix $\rho_{tot}(\lambda_s, \lambda_i)$ ($\rho_{tot}(\omega_s, \omega_i)$) in the signal-idler wavelength (frequency) space following a similar as [12], while accounting for all the multi-FWM contributions. Using spectral

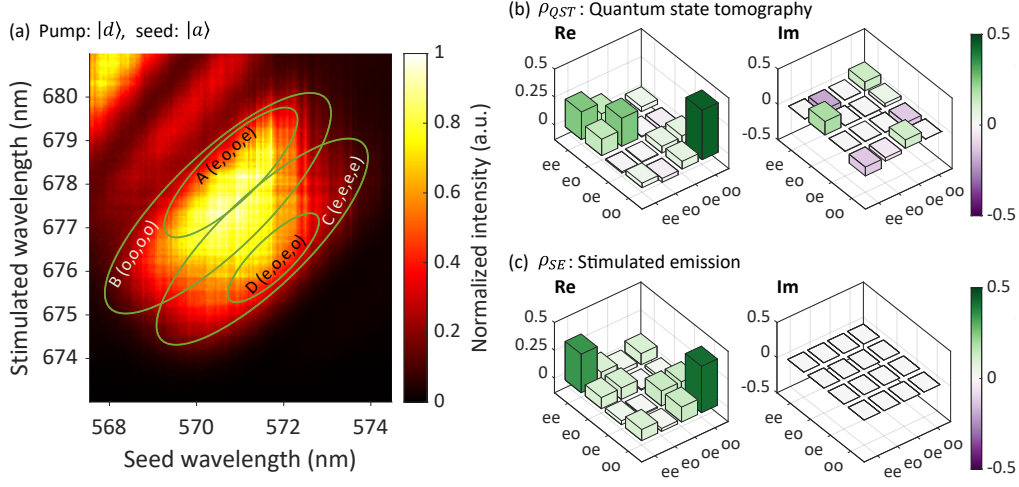


Fig. 6. (a) JSI plot of a 2.5 cm \times 2 orthogonally-spliced PMF with the pump in $|d\rangle$ and seed in $|a\rangle$. The $1/e^2$ contours (solid lines) of the two-dimensional Gaussian fits for $(T_{p1}, T_{p2}, T_s, T_i)$ processes are shown. The corresponding transverse-mode quantum state in density matrices (b) ρ_{QST} measured with a transverse-mode quantum state tomography (QST) and (c) ρ_{SE} estimated from the stimulated-emission measurement results in (a). The fidelities between the two density matrices are $F(\rho_{QST}, \rho_{SE}) = 0.73$ and $F(|\rho_{QST}|, \rho_{SE}) = 0.85$.

decomposition [56], the full density matrix at given signal and idler wavelengths can be calculated as $\rho_{Tot}(\lambda_s, \lambda_i) = \sum_j m_j \rho_j(\lambda_s, \lambda_i)$ where $m_j \geq 0$, $\sum_j m_j = 1$. This means that a point in the signal-idler wavelength space (λ_s, λ_i) can be represented as a linear combination of density matrices ρ_j 's, where each $\rho_j = |\psi_j\rangle\langle\psi_j|$ describes a pure quantum state $|\psi_j\rangle$ of a specific FWM-process combination. For example, ρ_B , ρ_C , and $\rho_{B \cap C}$ represent $|\psi_B\rangle = C_B \otimes |oo\rangle_B$, $|\psi_C\rangle = C_C \otimes |ee\rangle_C$, and $|\psi_{B \cap C}\rangle = C_C \otimes |ee\rangle_C + C_B \otimes |oo\rangle_B$, respectively. In general, if N -FWM processes exist, there will be $2^N - 1$ binary combinations of ρ_j 's that specify whether a given signal-idler wavelength point lies inside or outside of a certain FWM process. Representing each FWM process with the two-dimensional Gaussian fitting functions as shown Fig. 6(a) helps us to numerically categorize and calculate the individual density matrices in the signal-idler wavelength domain. Then, in the given signal- and idler-spectral windows defined by interference filters, we integrate all these point-wise density matrices to produce a single transverse-mode density matrix over that spectral range. In other words, the reduced density matrix in the transverse-mode domain, ρ_{Tot}^T where the frequency DOF is traced out, is calculated by integrating over all the density matrices across a given spectral window: $\rho_{SE} = \rho_{Tot}^T = \text{tr}_\lambda(\rho_{Tot}(\lambda_s, \lambda_i)) = \int d\lambda_s d\lambda_i \rho_{Tot}(\lambda_s, \lambda_i)$.

Fig. 6(c) shows the ρ_{SE} density matrix result from this calculation with a spectral window modeled after the interference filter setting used in the QST measurement ($\lambda_i = [567.5, 574.5]$ nm, $\lambda_s = [673.0, 681.0]$ nm). ρ_{SE} estimates concurrence = 0.00, Bell fidelity = 0.48, and purity = 0.40. The stimulated-emission-derived density matrix ρ_{SE} shows good qualitative similarity with the transverse-mode quantum state tomography result ρ_{QST} in Fig. 6(b) by having similar trend in the relative intensities of the density matrix elements – high $|ee\rangle\langle ee|$ and $|oo\rangle\langle oo|$, non-zero $|ee\rangle\langle oo|$ and $|oo\rangle\langle ee|$ coherent interaction elements, and other residual elements. Quantitatively, the fidelity F that describes the degree of similarity between two density matrices is $F(\rho_{QST}, \rho_{SE}) = 0.73$ for the QST-measured and the stimulated-emission-estimated states. ρ_{SE} estimation is closer if the phase information can be ignored, i.e., $F(|\rho_{QST}|, \rho_{SE}) = 0.85$,

which is related to the current phase measurement limitation of our method as shall be discussed later.

Despite the remaining discrepancies, ρ_{SE} provides the reasoning behind the low transverse-mode entanglement, which is challenging to assess solely based on the ρ_{QST} result: some distinguishabilities exist outside the transverse-mode DOF, specifically in the spectral DOF. Within the given spectral window, the imperfect spectral overlap between the processes B and C and the presence of other processes A and D indeed contribute to the ρ_{SE} (ρ_{QST}) matrix elements and thus to the low transverse-mode entanglement. Moreover, since we can choose an arbitrary spectral window to calculate ρ_{SE} , we can also hypothesize that in order to improve the entanglement, a narrower spectral filters that can isolate the B-C intersection area or a phase-matching engineering [57] to increase the B-C overlap while decreasing the A-D intervention can be beneficial.

5.2. Discussion on possible improvements

The aforementioned difference in quantitative measures (purity, concurrence, and Bell fidelity) between ρ_{QST} and ρ_{SE} can be explained by the following assumptions made in the calculation, which may improve with adequate treatments. First, we assume a Gaussian instead of the original phase-matching functions [42] for fitting the JSI. As the sinc (degenerate pump) and the complex error functions (non-degenerate pump) describe the phase matching function more accurately according to Sec. 2.3, a Gaussian function can underestimate the spectral overlap that may originate from the sinc and the non-degenerate pump function tails extending outwards [1], reducing the overall entanglement. Fitting with more precise phase matching functions will help resolve this issue. Second, we assume a flat joint spectral phase (JSP) for all the FWM processes involved. This lack of phase information can explain why the imaginary part of the ρ_{SE} is zero even though that of ρ_{QST} is not. Nonetheless, the analysis can be easily extended to a non-zero JSP case given that a JSP can be measured with previously studied methods as in [1, 26]. Then, the phase of a FWM process will be determined by the corresponding JSP, i.e., $c_j \propto f_j \propto e^{i(JSP)}$ (see Eq. 3 and Supplement 1 for more details). Third, we assume no other distinguishabilities exist besides transverse mode and frequency that can undermine the transverse-mode entanglement. Although the linear polarizers and a cross-spliced fiber help compensate any polarization and temporal distinguishabilities remaining in the system (the second PMF in the cross-spliced PMF corrects for polarization- and transverse-mode parity-dependent temporal walk-offs introduced in the first PMF [50]), there is a chance that unaccounted distinguishabilities remain. As a remedy, extending the technique to other DOFs may be helpful [12, 58].

In addition, the accuracy and functionality of the estimation can be further improved by: incorporating the raw JSI data (instead of the fit) of individual FWM processes by exciting one process at a time, conducting a frequency-resolved transverse-mode stimulated emission tomography, which naturally accounts for all possible distinguishabilities, and leading for an improvement of the numerical model used in the previous works [8–10] to predict the quantum state without conducting an experiment.

Despite the current limitations, stimulated-emission can characterize a FWM photon-pair source for its transverse-mode-frequency information and provide a quick estimation of the quantum state (5 projective measurements, compared to 36 for the standard QST) with reasonable agreement to that from a QST. Compared to the QST, which often requires longer measurement and more careful experimental treatment, including increasingly higher number of projection measurements required as the dimension increases (also applies to stimulated emission tomography), our stimulated-emission estimation may be suitable for initial multi-mode, multi-DOF entanglement source engineering. Thus, this JSI-based estimation of a density matrix may have a good potential as an effective tool for diagnosing and optimizing the entanglement source while minimizing the measurement resource used.

6. Conclusion

Using the stimulated-emission characterization technique described, we demonstrated its capability to reveal the transverse-mode-frequency relation of the photon pairs created from four-wave mixing processes in few-mode PMF. We measured the joint spectral intensities (JSIs) and transverse modes of the stimulated signal while varying the pump and seed transverse modes, as well as the seed wavelength. As a result, we identified the corresponding FWM processes predicted by the theory and the additional parity birefringence dispersion parameter, δ , needed to describe the experimental results. We demonstrated the efficiency of our technique by comparing with the spontaneous counterpart for the exposure time and contrast to exhibit a comparable spatial feature in imaging the signal transverse mode. With the effectiveness of our stimulated-emission measurement, not only did we demonstrate the real-time imaging capability, but also applied the technique to a fiber-based photon-pair source with a partial transverse-mode entanglement. We illustrated how the transverse-mode quantum state of the photon pairs can be estimated from the transverse-mode-resolved stimulated JSIs, when multiple spectrally overlapping FWM processes coexist. The estimated density matrix ρ_{SE} showed good qualitative agreement with that measured from a standard transverse-mode QST, ρ_{QST} , allowing us to diagnose the potential cause of entanglement degradation.

Likewise, we believe that our stimulated-emission-based transverse-mode-frequency characterization technique will be a useful experimental tool to efficiently estimate and optimize the quantum state when the design of a multi-variable photon-pair source and optimization of its entanglement is crucial. Indeed, a similar analysis can be conducted in a variety of quantum systems beyond few-mode PMF with a higher dimension [59–62] or different degrees of freedom [12]. The technique may also benefit from a possible extension to a spectrally-resolved transverse-mode stimulated-emission tomography [12, 23, 25] and joint spectral phase measurement [1, 26]. Greatly reducing the single-photon-level measurement effort to assess the generated photon-pair state for entanglement, we foresee a future where our stimulated-emission characterization method can be utilized to create versatile fiber-based photon-pair source capable of multi-modal frequency, transverse-mode entanglements, as well as transverse-mode-frequency hybrid-entanglement generation.

7. Supplement 1

7.1. Detailed quantum state representations

Quantum state of the pump,

$$|\psi_p\rangle = \sum_j \int d\omega_p a_j |\omega_p, T_p, x, \dots\rangle_j = \sum_j A_j \otimes |T_p\rangle_j, \quad (6)$$

$$|\psi_{p_1 p_2}\rangle = |\psi_p\rangle^{\otimes 2} = \sum_j \int d\omega_p^2 b_j |\omega_p \omega_p, T_{p_1} T_{p_2}, xx, \dots\rangle_j = \sum_j B_j \otimes |T_{p_1} T_{p_2}\rangle_j \quad (7)$$

where the prefactors satisfying the pump condition $|\psi_p\rangle = |\psi_{p_1}\rangle = |\psi_{p_2}\rangle$ (given that we do not have individual control over the two pumps) are

$$a_j = M_{a_j} \alpha(\omega_p), \quad A_j = \int d\omega_p a_j |\omega_p, x, \dots\rangle_j, \quad (8)$$

$$b_j = M_{b_j} \alpha^2(\omega_p) = a_j^2, \quad B_j = \int d\omega_p^2 b_j |\omega_p \omega_p, xx, \dots\rangle_j \quad (9)$$

Here, M_{a_j} and M_{b_j} are (complex) coefficients that depend on the relative amplitude and phase of different pump (transverse) modes, satisfying $\langle \psi_{p_1 p_2} | \psi_{p_1 p_2} \rangle = 1$ and $\langle \psi_p | \psi_p \rangle = 1$.

Quantum state of the signal-idler photon pair,

$$|\psi_{si}\rangle = \sum_j^N \int d\omega_s d\omega_i c_j |\omega_s \omega_i, T_s T_i, yy, \dots\rangle_j = \sum_j^N C_j \otimes |T_s T_i\rangle_j, \quad (10)$$

where the prefactors are

$$c_j = M_{c_j} b_j f_j(\omega_s, \omega_i) O_j(T_{p_1}, T_{p_2}, T_s, T_i), \quad C_j = \int d\omega_s d\omega_i c_j |\omega_s \omega_i, yy, \dots\rangle_j. \quad (11)$$

Notice that $\sqrt{P_{p_1 j} P_{p_2 j}}$ in Eq. 3, which varies with the transverse modes and frequencies involved in the process j , is replaced with b_j to more accurately reflect the pump contribution.

Joint spectral amplitude (JSA),

$$f_j(\omega_s, \omega_i) = |f_j(\omega_s, \omega_i)| e^{i \arg\{f_j(\omega_s, \omega_i)\}} = \sqrt{\text{JSI}} e^{i(\text{JSP})}, \quad (12)$$

where the definitions, joint spectral intensity $\text{JSI} = |f_j(\omega_s, \omega_i)|^2$ and joint spectral phase $\text{JSP} = \arg\{f_j(\omega_s, \omega_i)\}$, are used.

Transverse-mode overlap integral,

$$O_j(T_{p_1}, T_{p_2}, T_s, T_i) = M_{o_j} \int d^2\vec{r} T_{p_1}(\vec{r}) T_{p_2}(\vec{r}) T_s^*(\vec{r}) T_i^*(\vec{r}), \quad (13)$$

where M_{o_j} is the normalization constant satisfying $\sum_j |O_j|^2 = 1$, \vec{r} the transverse position, and $T_\nu(\vec{r})$ the transverse electric field of photon ν .

7.2. Seed laser calibration

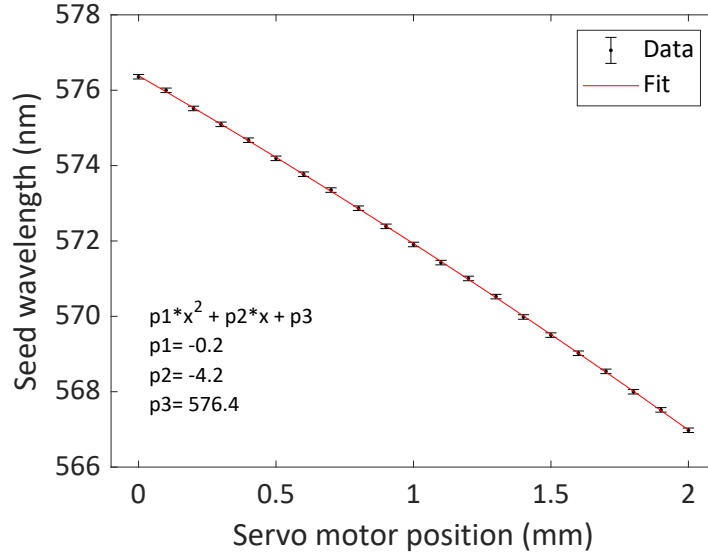


Fig. 7. Calibration curve of the dye (seed) laser in servo motor steps of 0.1 mm specified by a quadratic fit. The seed is calibrated by measuring its center wavelength as a function of the DC servo motor (Thorlabs Z812B) position, which is responsible for the wavelength tuning (rotates the birefringent filters in the laser cavity) of the dye laser.

7.3. Animated and real-time video results

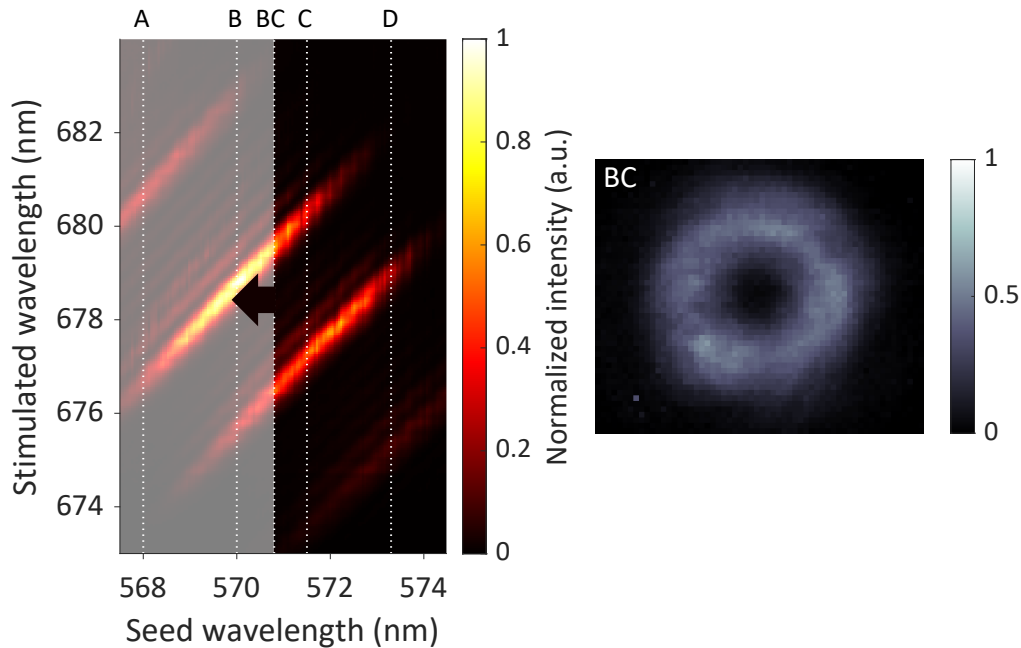


Fig. 8. Screenshot of an animated video Visualization 1 illustrating the continuous evolution of the stimulated signal transverse mode as the seed wavelength is scanned. The JSI is horizontally scanned with the seed wavelength (left) as the corresponding stimulated image is shown simultaneously (right). The center seed (idler) wavelengths and the corresponding stimulated (signal) transverse mode images are labeled with the FWM processes (A-D). Notice that BC is located in the middle of the two processes, B and C. This animation is recreated from two separate measurements of a JSI and individual stimulated beam images each taken with 400 ms exposure time. The images are background subtracted and normalized in intensity.

Funding. National Science Foundation (1806572, 1640968, 1839177, 2207822); U.S. Department of Energy, Office of Science, Biological and Environmental Research program (Award No. DE-SC0023167).

Acknowledgments. We thank Joel Carpenter for help with transverse-mode control using an SLM, Elizabeth Goldschmidt for help with aligning the CW dye laser, Oliver Wang and Xinan Chen for the initial experimental setup, Offir Cohen and Bin Fang for helpful discussion about density matrix error analysis, Xiao Liu, Daniel Shahaar, and Siddharth Ramachandran for useful discussion about OAM modes, and Soho Shim with fruitful discussion about simplifying explanation for the overall concept.

Disclosures. The authors declare no conflicts of interest.

Data Availability Statement. Data underlying the results presented in this paper are not publicly available at this time but may be obtained from the authors upon reasonable request.

Supplemental document. See Supplement 1 for supporting content.

References

1. K. Garay-Palmett, D. B. Kim, Y. Zhang, *et al.*, “Fiber-based photon-pair generation: tutorial,” *J. Opt. Soc. Am. B* **40**, 469–490 (2023).
2. A. Anwar, C. Perumangatt, F. Steinlechner, *et al.*, “Entangled photon-pair sources based on three-wave mixing in bulk crystals,” *Rev. Sci. Instruments* **92**, 041101 (2021).
3. A. E. Willner, “Oam light for communications,” *Opt. Photonics News* **32**, 34–41 (2021).
4. M. Hiekkamäki and R. Fickler, “High-dimensional two-photon interference effects in spatial modes,” *Phys. Rev. Lett.* **126**, 123601 (2021).

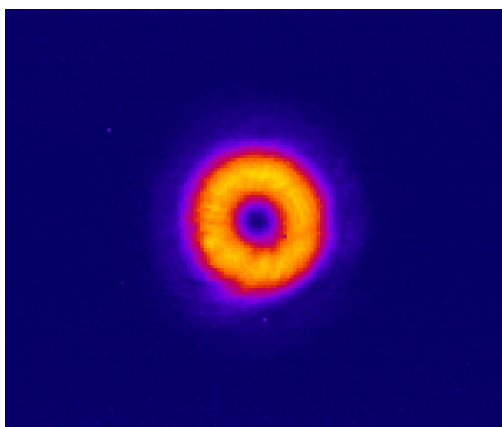


Fig. 9. Screenshot of a real-time video Visualization 2. This raw video data shows in real-time, how the transverse mode of the stimulated beam changes as the seed wavelength (servo motor) is scanned. Exposure time for this video is kept the same as the Fig. 8, 400 ms. A difference is that this video shows a $152 \text{ px} \times 128 \text{ px}$ full field of view, while others (Fig. 3, 5, and Vid. 8) are trimmed to the $60 \text{ px} \times 50 \text{ px}$ region of interest.

5. T. Gregory, P.-A. Moreau, E. Toninelli, and M. J. Padgett, "Imaging through noise with quantum illumination," *Sci. advances* **6**, eaay2652 (2020).
6. R. S. Aspden, N. R. Gemmell, P. A. Morris, *et al.*, "Photon-sparse microscopy: visible light imaging using infrared illumination," *Optica* **2**, 1049–1052 (2015).
7. P.-A. Moreau, E. Toninelli, T. Gregory, and M. J. Padgett, "Ghost imaging using optical correlations," *Laser & Photonics Rev.* **12**, 1700143 (2018).
8. D. Cruz-Delgado, R. Ramirez-Alarcon, E. Ortiz-Ricardo, *et al.*, "Fiber-based photon-pair source capable of hybrid entanglement in frequency and transverse mode, controllably scalable to higher dimensions," *Sci. reports* **6**, 1–9 (2016).
9. K. Garay-Palmett, D. Cruz-Delgado, F. Dominguez-Serna, *et al.*, "Photon-pair generation by intermodal spontaneous four-wave mixing in birefringent, weakly guiding optical fibers," *Phys. Rev. A* **93**, 033810 (2016).
10. D. Cruz-Delgado, J. Monroy-Ruz, A. M. Barragan, *et al.*, "Configurable spatiotemporal properties in a photon-pair source based on spontaneous four-wave mixing with multiple transverse modes," *Opt. Lett.* **39**, 3583–3586 (2014).
11. K. Zielnicki, K. Garay-Palmett, D. Cruz-Delgado, *et al.*, "Joint spectral characterization of photon-pair sources," *J. Mod. Opt.* **65**, 1141–1160 (2018).
12. B. Fang, M. Liscidini, J. Sipe, and V. Lorenz, "Multidimensional characterization of an entangled photon-pair source via stimulated emission tomography," *Opt. express* **24**, 10013–10019 (2016).
13. J. B. Altepeter, E. R. Jeffrey, and P. G. Kwiat, "Photonic state tomography," *Adv. At. Mol. Opt. Phys.* **52**, 105–159 (2005).
14. J. T. Barreiro, N. K. Langford, N. A. Peters, and P. G. Kwiat, "Generation of hyperentangled photon pairs," *Phys. review letters* **95**, 260501 (2005).
15. M. Rambach, M. Qaryan, M. Kewming, *et al.*, "Robust and efficient high-dimensional quantum state tomography," *Phys. Rev. Lett.* **126**, 100402 (2021).
16. F. Huszár and N. M. Houlby, "Adaptive bayesian quantum tomography," *Phys. Rev. A* **85**, 052120 (2012).
17. D. H. Mahler, L. A. Rozema, A. Darabi, *et al.*, "Adaptive quantum state tomography improves accuracy quadratically," *Phys. review letters* **111**, 183601 (2013).
18. C. Ferrie, "Self-guided quantum tomography," *Phys. review letters* **113**, 190404 (2014).
19. D. Gross, Y.-K. Liu, S. T. Flammia, *et al.*, "Quantum state tomography via compressed sensing," *Phys. review letters* **105**, 150401 (2010).
20. F. Bouchard, D. Koutnỳ, F. Hufnagel, *et al.*, "Compressed sensing of twisted photons," *Opt. Express* **27**, 17426–17434 (2019).
21. F. Bouchard, N. H. Valencia, F. Brandt, *et al.*, "Measuring azimuthal and radial modes of photons," *Opt. express* **26**, 31925–31941 (2018).
22. D. Zia, N. Dehghan, A. D'Errico, *et al.*, "Interferometric imaging of amplitude and phase of spatial biphoton states," *Nat. Photonics* pp. 1–8 (2023).
23. M. Liscidini and J. Sipe, "Stimulated emission tomography," *Phys. review letters* **111**, 193602 (2013).

24. B. Fang, O. Cohen, M. Liscidini, *et al.*, “Fast and highly resolved capture of the joint spectral density of photon pairs,” *Optica* **1**, 281–284 (2014).
25. L. A. Rozema, C. Wang, D. H. Mahler, *et al.*, “Characterizing an entangled-photon source with classical detectors and measurements,” *Optica* **2**, 430–433 (2015).
26. G. Thekkadath, B. Bell, R. Patel, *et al.*, “Measuring the joint spectral mode of photon pairs using intensity interferometry,” *Phys. Rev. Lett.* **128**, 023601 (2022).
27. D. Caetano, M. Almeida, P. S. Ribeiro, *et al.*, “Conservation of orbital angular momentum in stimulated down-conversion,” *Phys. Rev. A* **66**, 041801 (2002).
28. A. de Oliveira, G. Santos, N. R. da Silva, *et al.*, “Beyond conservation of orbital angular momentum in stimulated parametric down-conversion,” *Phys. Rev. Appl.* **16**, 044019 (2021).
29. A. G. de Oliveira, M. F. Arruda, W. C. Soares, *et al.*, “Real-time phase conjugation of vector vortex beams,” *ACS Photonics* **7**, 249–255 (2019).
30. Y. Xu, S. Choudhary, and R. W. Boyd, “Efficient measurement of the bi-photon spatial mode entanglement with stimulated emission tomography,” arXiv preprint arXiv:2403.05036 (2024).
31. M. A. Ciampini, A. Gherardi, V. Cimini, *et al.*, “Stimulated emission tomography: beyond polarization,” *Opt. Lett.* **44**, 41–44 (2019).
32. D. Kim, X. Hu, Y. Zhang, *et al.*, “Stimulated-emission-based characterization of optical fiber photon-pair source in frequency and transverse mode,” in *Frontiers in Optics*, (Optica Publishing Group, 2020), pp. JM6B–22.
33. J. Carpenter, B. C. Thomsen, and T. D. Wilkinson, “Degenerate mode-group division multiplexing,” *J. Light. Technol.* **30**, 3946–3952 (2012).
34. J. Carpenter, B. J. Eggleton, and J. Schröder, “Complete spatiotemporal characterization and optical transfer matrix inversion of a 420 mode fiber,” *Opt. Lett.* **41**, 5580–5583 (2016).
35. N. K. Fontaine, R. Ryf, H. Chen, *et al.*, “Laguerre-gaussian mode sorter,” *Nat. Communications* **10**, 1–7 (2019).
36. A. Mair, A. Vaziri, G. Weihs, and A. Zeilinger, “Entanglement of the orbital angular momentum states of photons,” *Nature* **412**, 313–316 (2001).
37. L.-T. Feng, M. Zhang, X. Xiong, *et al.*, “On-chip transverse-mode entangled photon pair source,” *npj Quantum Inf.* **5**, 1–7 (2019).
38. Ç. Ekici and M. S. Dinleyici, “Graded-index optical fiber transverse-spatial-mode entanglement,” *Phys. Rev. A* **102**, 013702 (2020).
39. K. Sulimany and Y. Bromberg, “All-fiber source and sorter for multimode correlated photons,” *npj Quantum Inf.* **8**, 1–5 (2022).
40. C. L. Morrison, F. Graffitti, P. Barrow, *et al.*, “Frequency-bin entanglement from domain-engineered down-conversion,” *APL Photonics* **7** (2022).
41. A. W. Snyder, J. D. Love *et al.*, *Optical waveguide theory*, vol. 175 (Chapman and hall London, 1983).
42. K. Garay-Palmett, H. McGuinness, O. Cohen, *et al.*, “Photon pair-state preparation with tailored spectral properties by spontaneous four-wave mixing in photonic-crystal fiber,” *Opt. Express* **15**, 14870–14886 (2007).
43. Q. Lin, F. Yaman, and G. P. Agrawal, “Photon-pair generation in optical fibers through four-wave mixing: Role of raman scattering and pump polarization,” *Phys. Rev. A* **75**, 023803 (2007).
44. B. J. Smith, P. Mahou, O. Cohen, *et al.*, “Photon pair generation in birefringent optical fibers,” *Opt. Express* **17**, 23589–23602 (2009).
45. K. Zielnicki, K. Garay-Palmett, R. Dirks, *et al.*, “Engineering of near-ir photon pairs to be factorable in space-time and entangled in polarization,” *Opt. Express* **23**, 7894–7907 (2015).
46. P. Boucher, H. Defienne, and S. Gigan, “Engineering spatial correlations of entangled photon pairs by pump beam shaping,” *Opt. Lett.* **46**, 4200–4203 (2021).
47. J. A. Davis, D. M. Cottrell, J. Campos, *et al.*, “Encoding amplitude information onto phase-only filters,” *Appl. Optics* **38**, 5004–5013 (1999).
48. G. Labroille, B. Denolle, P. Jian, *et al.*, “Efficient and mode selective spatial mode multiplexer based on multi-plane light conversion,” *Opt. Express* **22**, 15599–15607 (2014).
49. M. Krenn, M. Malik, M. Erhard, and A. Zeilinger, “Orbital angular momentum of photons and the entanglement of laguerre–gaussian modes,” *Philos. Trans. Royal Soc. A: Math. Phys. Eng. Sci.* **375**, 20150442 (2017).
50. E. Meyer-Scott, V. Roy, J.-P. Bourgoin, *et al.*, “Generating polarization-entangled photon pairs using cross-spliced birefringent fibers,” *Opt. Express* **21**, 6205–6212 (2013).
51. D. B. Kim, A. B. U’ren, K. Garay-Palmett, and V. O. Lorenz, “Generating transverse-mode entanglement in optical fiber,” in *Quantum Computing, Communication, and Simulation III*, vol. 12446 (SPIE, 2023), pp. 174–176.
52. D. B. Kim, A. B. U’Ren, K. Garay-Palmett, and V. O. Lorenz, “Towards transverse-mode entanglement generation in few-mode optical fiber,” in *Quantum 2.0*, (Optica Publishing Group, 2023), pp. QW2A–19.
53. M. Agnew, J. Leach, M. McLaren, *et al.*, “Tomography of the quantum state of photons entangled in high dimensions,” *Phys. Rev. A* **84**, 062101 (2011).
54. N. K. Langford, R. B. Dalton, M. D. Harvey, *et al.*, “Measuring entangled qutrits and their use for quantum bit commitment,” *Phys. Review Letters* **93**, 053601 (2004).
55. M. Hiekkamäki, S. Prabhakar, and R. Fickler, “Near-perfect measuring of full-field transverse-spatial modes of light,” *Opt. Express* **27**, 31456–31464 (2019).
56. M. A. Nielsen and I. L. Chuang, *Quantum Computation and Quantum Information: 10th Anniversary Edition*

(Cambridge University Press, 2010).

57. X. Liu, D. B. Kim, V. O. Lorenz, and S. Ramachandran, "Engineering joint spectral densities with orbital angular momentum states in optical fibers," in *CLEO: QELS Fundamental Science*, (Optica Publishing Group, 2022), pp. FF2J-1.
58. M. Plöschner, M. M. Morote, D. S. Dahl, *et al.*, "Spatial tomography of light resolved in time, spectrum, and polarisation," *Nat. Commun.* **13**, 4294 (2022).
59. N. Bozinovic, Y. Yue, Y. Ren, *et al.*, "Terabit-scale orbital angular momentum mode division multiplexing in fibers," *science* **340**, 1545-1548 (2013).
60. S. Ramachandran, P. Gregg, P. Kristensen, and S. Golowich, "On the scalability of ring fiber designs for oam multiplexing," *Opt. express* **23**, 3721-3730 (2015).
61. H. Defienne, M. Barbieri, I. A. Walmsley, *et al.*, "Two-photon quantum walk in a multimode fiber," *Sci. advances* **2**, e1501054 (2016).
62. D. I. Shahaar, X. Liu, D. B. Kim, *et al.*, "Photon pair generation in oam modes at 780 and 1550 nm via spontaneous intermodal four wave mixing," in *CLEO: Fundamental Science*, (Optica Publishing Group, 2023), pp. FF1L-5.